Extreme climate after massive eruption of Alaska's Okmok volcano in 43 BCE and effects on the late Roman Republic and Ptolemaic Kingdom

Joseph R. McConnell[1,2,*], Michael Sigl[3], Gill Plunkett[4], Andrea Burke[5], Woon Mi Kim[3], Christoph C. Raible[3,4], Andrew I. Wilson[6,7], Joseph G. Manning[8], Francis Ludlow[9], Nathan J. Chellman[1], Helen M. Innes[5], Zhen Yang[9], Jessica F. Larsen[10], Janet R. Schaefer[11], Sepp Kipfstuhl[12], Seyedhamidreza Mojtabavi[12,13], Frank Wilhelms[12,13], Thomas Opel[12], Hanno Meyer[12], Jørgen Peder Steffensen[14]

[1]Division of Hydrologic Sciences, Desert Research Institute, 89512, USA

[2]Sir Nicholas Shackleton Visiting Fellow, Clare Hall, University of Cambridge, CB3 9AL, UK

[3]Climate and Environmental Physics, Physics Institute, and Oeschger Centre for Climate Change Research, University of Bern, CH-3012, Switzerland

[4]School of Natural and Built Environment, Queen's University Belfast, BT7 1NN, UK

[5]School of Earth and Environmental Sciences, University of St Andrews, UK

[6]Faculty of Classics, University of Oxford, OX1 3LU, UK

[7]School of Archaeology, University of Oxford, OX1 3TG, UK

[8]Department of History & Classics and School of Forestry & Environmental Studies, Yale University, 06520-8266, USA

[9]Trinity Centre for Environmental Humanities, Department of History, School of Histories & Humanities, Trinity College, Dublin 2 Ireland.

[10]Department of Geosciences, University of Alaska Fairbanks, 99775, USA

[11]State of Alaska Division of Geological and Geophysical Surveys, 99709, USA

[12]Alfred-Wegener-Institut Helmholtz-Zentrum für Polar- und Meeresforschung, 27570 Bremerhaven and 14473 Potsdam, Germany

[13]Department of Crystallography, Geoscience Centre, University of Göttingen, 37073, Germany

[14]Physics of Ice, Climate, and Earth, University of Copenhagen, DK-1017, Denmark

Classification

Physical Sciences/Earth, Atmospheric, and Planetary Sciences; Social Sciences/Economic Sciences

Corresponding Author

Joseph R. McConnell, Desert Research Institute, 2215 Raggio Parkway, Reno NV 89512 USA (Email: Joe.McConnell@dri.edu; Phone: 775-673-7348; Fax: 775-673-7363)

Abstract

The assassination of Julius Caesar in 44 BCE triggered a power struggle that ultimately ended the Roman Republic and, eventually, the Ptolemaic Kingdom, leading to the rise of the Roman Empire. Climate proxies and written documents indicate that this struggle occurred during a period of unusually inclement weather, famine, and disease in the Mediterranean region; historians have previously speculated that a large volcanic eruption of unknown origin was the most likely cause. Here we show using well-dated volcanic fallout records in six Arctic ice cores that one of the largest volcanic eruptions of the past 2,500 years occurred in early 43 BCE, with distinct geochemistry of tephra deposited during the event identifying the Okmok volcano in Alaska as the source. Climate proxy records show that 43 and 42 BCE were among the coldest years of recent millennia in the Northern Hemisphere at the start of one of the coldest decades. Earth system modeling suggests that radiative forcing from this massive, high-latitude eruption led to pronounced changes in hydroclimate, including seasonal temperatures in specific Mediterranean regions as much as 7°C below normal during the two-year period following the eruption, and unusually wet conditions. While it is difficult to establish direct causal linkages to thinly documented historical events, the wet and very cold conditions from this massive eruption on the opposite side of Earth probably resulted in crop failures, famine, and disease, exacerbating social unrest and contributing to political realignments throughout the Mediterranean region at this critical juncture of Western civilization.

Significance Statement

The first-century BCE fall of the Roman Republic and Ptolemaic Kingdom, and subsequent rise of the Roman Empire were among the most important political transitions in the history of Western civilization. Volcanic fallout in well-dated Arctic ice-core records, climate proxies, and Earth system modeling show that this transition occurred during an extreme cold period resulting from a massive eruption of Alaska's Okmok volcano early in 43 BCE. Written sources describe unusual climate, crop failures, famine, disease, and unrest in the Mediterranean immediately following the eruption— suggesting significant vulnerability to sudden hydroclimatic shocks in otherwise sophisticated and powerful ancient states. Such shocks

must be seen as having played a role in the historical developments for which the period is famed.

The assassination of Julius Caesar on the Ides of March in 44 BCE marked the beginning of a 17-year struggle for the future of the greater Mediterranean region — including the Roman Republic and Ptolemaic Egyptian Kingdom — that culminated with the rise of the Roman Empire. Although it is sometimes difficult to separate fact from myth associated with these transformative events, the thin surviving historical accounts credibly describe unusual atmospheric phenomena in the Mediterranean region from 44 BCE and China from 43 BCE (1), as well as anomalously inclement weather (2) and widespread famine (3) that provide a notable environmental background important to understanding the period's reorganization of political power that ultimately changed the course of history (4). Northern Hemisphere (NH) climate proxies show that 43 and 42 BCE were among the coldest of the past 2,500 years, coincident with the start of one of the coldest decades (5, 6), although no annually resolved climate proxy records exist for the Mediterranean region specifically. Moreover, ice-core records of lead pollution in northcentral Greenland — a proxy of European lead/silver mining and smelting during antiquity and already low during the Crisis of the Roman Republic (7, 8) — declined during this decade suggesting further deterioration of the Roman economy. Historians and scientists who study these ancient times have speculated that a large volcanic eruption most likely was the cause of these unusual atmospheric and climate events, although uncertain chronologies and low resolution in the available ice-core and other records have to date limited understanding of the magnitude and extent of the climate anomaly and therefore its potential effects on ancient societies. Speculation based primarily on the approximate timing and magnitude of known NH eruptions during this period suggested the most likely source volcano was Mt. Etna (2) in Sicily or Shiveluch (9) in Kamchatka, with more recent speculation focused on Nicaragua's Apoyeque (5, 10).

Ice-core evidence of a massive eruption in early 43 BCE

We used records of volcanic fallout in six Arctic ice cores (Fig. 1; SI Appendix, Fig. S1) — all synchronized to the same annual-layer-counted and verified time scale (7) — as well as climate proxies and Earth system modeling to develop a more complete understanding of the

timing and magnitude of volcanism during this period and its effects on climate and history. We focused our interpretation on new, high-resolution measurements of volcanic fallout (Materials and Methods) in the North Greenland Ice Core Project 2 (NGRIP2) core on the recently developed and verified Desert Research Institute (DRI)_NGRIP2 age scale that provide the most detailed and well-dated records of volcanic fallout for this period (Fig. 2) (7). Age uncertainties for this age scale previously were shown to be less than ±2 years during antiquity (7), although the exact coincidence between the massive fallout of radiatively important non-sea-salt sulfur (nssS) measured in NGRIP2 and the pronounced temperature anomaly in absolutely dated tree-ring records (5) implies no dating uncertainty in the ice chronology at 43 BCE (Fig. 2). Throughout this study, 43 BCE corresponds to the period between 1991 and 1992 years before 1950 (ybp) (SI Appendix, Table S1).

The NGRIP2 measurements clearly delineate volcanic fallout from two distinct eruptions: the first starting in early (i.e., January or February) 45 BCE and the second in early 43 BCE. The nssS fallout from the first eruption suggests it was a powerful but short-lived event, with fallout returning to background levels by late 45 BCE. Comparisons to the array of four other Greenland ice-core records (SI Appendix, Fig. S1) show that fallout from the 45 BCE event was confined largely to northern Greenland, suggesting a nearby high-latitude source volcano (e.g., Iceland). In addition, proxy records (6) indicate no large-scale climate effects so it is unlikely that this eruption had a significant influence on the mid-latitude regions. The nssS fallout from the second event suggests that it was a massive eruption that started in early 43 BCE, with elevated volcanic fallout lasting more than two years. Increased nssS concentrations started in the NGRIP2 record in early winter, reached a temporary peak in spring and an overall maximum in late autumn of 43 BCE, before returning to background concentrations by spring 41 BCE (Fig. 2). Sulfur isotope ratios measured in fallout from the beginning of the 43 BCE event in Greenland Ice Sheet Project 2 (GISP2) ice (Materials and Methods) showed non-zero $\Delta^{33}S$ values (SI Appendix, Fig. S3) that result from oxidation in a high-ultraviolet (UV) environment consistent with plume ejection above the ozone layer in the lower stratosphere (11). Injection into the stratosphere is consistent with persistent, widespread climate effects.

Comparisons of volcanic acid deposition recorded in the five Greenland cores indicate moderately greater fallout in central Greenland during the 43 BCE event, contrasting with the 45 BCE event. Fallout deposition during the two-year period was ~123 and ~110 kg/km^2 as sulfuric acid in the northern NGRIP2 and NEEM cores, and ~131 , ~135, and ~128 kg/km^2 in the GISP2 (12), GRIP (13), and Dye3 (13) cores to the south, respectively (Materials and Methods). In all six Arctic ice-core records (Fig. 1), the 43 BCE event ranked among the largest observed during the past 2,500 years for acid-equivalent deposition. For example, it ranked 2nd in NEEM (5), 3rd in GRIP (13), 2nd in GISP2 (12), 4th in Dye 3 (13), and 1st in the combined NGRIP (14) and NGRIP2 (this study) nssS record for the past 2,500 years. Similarly, average nssS for the two-year period of 43 and 42 BCE ranked 4th highest in the Russian Arctic (Akademii Nauk) ice-core record (this study) from 500 BCE up to the Industrial Revolution and the start of widespread industrial sulfur pollution.

Volcanic provenance

A sharp spike in 2.5 to 10 μm insoluble particle concentrations in NGRIP2, and in laser-light-scattering measurements in GISP2 (15), coincided with the early stages of the 43 BCE volcanic nssS peak suggesting deposition of volcanic tephra (16, 17) near the start of the eruption (Fig. 2; SI Appendix, Fig. S1). Microprobe analyses (Materials and Methods) of 35 volcanic shards (SI Appendix, Fig. S4) filtered from corresponding GISP2 ice revealed geochemical characteristics (Fig. 3; SI Appendix Fig. S5) matching reference tephra from the andesite fall and pyroclastic density current units from the caldera-forming, Volcanic Explosivity Index (VEI) 6, Okmok II (53.4°N, 168.1°W) eruption in Alaska (Fig. 1). The 43 BCE eruption date from Greenland ice cores is consistent with the 190 BCE to 50 CE (2σ, updated to IntCal13) (18) calibrated age range indicated by radiocarbon dates for organic material in the layers just below the initial proximal deposits of Okmok II. The geochemistry of the GISP2 shards and Okmok II reference tephra clearly is distinct from reference tephra from other potential volcanic eruptions in the 1st century BCE (Fig. 3; SI Appendix, Fig. S5) providing nearly unambiguous evidence that the Okmok II eruption was the source of the 43 BCE event. The precise identification of the source location now provides a key input in efforts to better model and understand the event's effects on climate.

Northern Hemisphere climate effects

The two-year cooling associated with the Okmok II eruption (Fig. 2) was among the most significant recorded in NH summer-temperature proxies for the past 2,500 years. For example, 43 and 42 BCE ranked as the 2nd and 8th coldest years in a recent tree-ring-based assessment (5), respectively, while the decade from 43 to 34 BCE was the fourth coldest. Central and northern European climate reconstructions based on measurements in temperature-sensitive trees from Scandinavia and Austria (6) indicate marked regional summertime cooling of >3°C and >2.5°C in 43 and 42 BCE (Fig. 2), respectively. Similarly, an annually dated speleothem record of summer temperatures from Shihua Cave in northeastern China shows a pronounced, three-year reduction in summertime temperature of >2.0°C starting in 45 BCE, coeval with 43 BCE within the 5 years dating uncertainty of the speleothem record (Fig. 2). A rare frost ring recorded in bristlecone pine trees from California's White Mountains indicates anomalous, below-freezing temperatures in early September 43 BCE (Fig. 2) during the late NH summer growing season (19).

Using the exact location, and the estimated eruption timing and sulfur yield of the Okmok II eruption, we used the Community Earth System Model (CESM, version 1.2.2) (20) to simulate the severity, extent, and persistence of the climate response (Fig. 2; Materials and Methods). The simulations indicate pronounced, widespread NH cooling in 43 and 42 BCE, with simulated summer air-temperature anomalies similar in magnitude and duration to the European tree-ring (21) and Chinese (Shihua Cave) speleothem (22) climate proxy records that show 2 to 3°C declines in summer air temperatures (Fig. 2). Chinese written records also document unusually cold weather in 43 and 42 BCE, including late spring and early autumn frosts (23). The CESM simulations suggest that cooling may have persisted into the early 30s BCE, as well as significant changes in global precipitation from the Okmok II eruption including increases over the Mediterranean region and strong decreases over Asia and the high NH latitudes (SI Appendix, Figs. S6, S7).

Climate effects and historical linkages in the Mediterranean region

Agreement between the few available annually resolved NH proxy records of summertime temperatures and the CESM-simulated temperature anomalies suggest that the model largely captures the temperature effects of radiative forcing associated with the early 43 BCE Okmok II eruption. Therefore, we used the simulated temperature and precipitation anomalies in the Roman provinces and Ptolemaic Kingdom (Fig. 4; SI Appendix, Figs. S8, S9) where no annually resolved climate proxies are available to investigate possible effects on ancient societies, though recognizing that accurately modeling precipitation is often particularly challenging. The effect of climate shocks on ancient societies most usually and directly occurred through diminished agricultural yields, with crop failures occurring because of insufficient or excessive rainfall at critical periods for plant growth (24), or because of unusual growing-season temperatures. The environmental perception of anomalous weather and other volcanically induced phenomena (e.g., visually spectacular dimming or discoloration of the solar disc) as portents also endowed these events with a significance that made their appearance politically influential in ancient societies.

The ice-core and climate-proxy record evidence, as well as the Earth system model simulations, suggest that the atmospheric and climate phenomena described by ancient Mediterranean sources and recently evaluated by historians (1-3) separate into two groups. The first cluster around March and April 44 BCE and consist of atmospheric phenomena (solar dimming, halos and parhelia) interpreted by ancient writers as signs and portents. Virgil, in his poem *Georgics* (1.466-73), said that the sun was darkened after Caesar's assassination, and the ancient commentator Servius added that "it is said, after Caesar had been killed in the Senate on the day before, the sun's light failed from the sixth hour until nightfall." Plutarch (*Life of Julius Caesar*, 69.3–4) said not only that the sun was veiled and pale, but also that it gave forth so little heat that fruits shrivelled rather than ripened. Several authors mentioned seeing three suns in the sky (Dio Cassius 45.17.5; Julius Obsequens 68; Eusebius *Chronicle*, Olympiad 184), a well-known phenomenon called 'sun-dogs' or parhelia caused by refraction of sunlight through ice crystals in the upper atmosphere in particularly cold weather. Dio and Obsequens added that there was a radiant colored halo around the sun, probably a "Bishop's Ring", a diffuse bluish-brown halo around the sun caused by sulfur-based aerosols from large volcanic

eruptions. Other writers mentioned a solar halo that marked Octavian's arrival in Rome in early April 44 BCE (e.g., Seneca, *NQ* 1.2.1; Suetonius, *Augustus* 95; Velleius Paterculus, 2.59.6; Pliny, *NH* 2.98; Dio Cassius 45.4.4; Obsequens 68; Orosius 6.20.5), and which was seized upon by Octavian and his supporters to suggest divine favor for his cause (1, 3). All these phenomena are consistent with the atmospheric effects of volcanic eruptions. However, given that they are reported as occurring before the probable date of the Okmok II eruption in 43 BCE, that all the sources referring to them originate in Italy or the central Mediterranean, and that NH proxies show no large-scale climate effects, the comparatively minor, historically well-documented eruption of Etna in 44 BCE is a plausible candidate for their cause.

The second group of ancient sources relates more directly to unusually cold weather and famine (3). These sources group from early 43 BCE to late 42 BCE and are consistent with the extreme climate effects (Fig. 4) of the massive, early 43 BCE Okmok II eruption indicated by volcanic fallout in the Arctic ice cores (Fig. 2). Although some sources suggest harsh winter weather in late 44 BCE, it is uncertain that these passages reflect especially unusual winters in the southern Balkans, or are more simply a commentary on the conditions that traditionally led armies to avoid movements in winter. Whether they also reflect the continuing after-effects of the relatively minor eruption of Etna in 44 BCE seven or eight months earlier is therefore similarly uncertain. Plutarch's *Life of Brutus* (25.2–4) mentioned that on his way to Epidamnus (modern Durrës, Albania), Brutus marched in late 44 BCE through snowstorms, and that he and his army suffered from *boulimia,* a disease brought on by fatigue, damp, and cold weather. Cicero, writing to Atticus in November 44 BCE referred to stormy weather (*Att*. 16.11). Two additional letters of Cicero in February 43 BCE (*Ad Fam*. 9.24.3 and 12.5.2), refer to winter and cold (after the early 43 BCE Okmok II eruption indicated in the ice-core records), and in a less-precisely dated passage, Josephus (*Jewish Antiquities* 14.310) wrote of Antonius in the winter of 44/43 BCE telling Hyrcanus about the severely cold climate of Macedonia (3).

More significant in registering the onset of major societal stress is a group of sources referring to famine in northern Italy in April 43 BCE and northern Greece in October 42 BCE, as well as additional reports of famine, food shortages, endemic disease, and civil unrest in Rome and other parts of Italy starting in 43 BCE and extending through 36 BCE (24). Plutarch in his *Life*

of Antony (17.3) wrote that the greatest of the various hardships faced by Antony and his army in flight after their defeat at Mutina in April 43 BCE was famine, the army being reduced to eating wild fruit, roots, bark and animals "never tasted before by men." Julius Obsequens (69) said that in 43 BCE a voice was heard at the oracle of Apollo (in Delphi, presumably), crying "Madness of wolves in the winter; in the summer the grain is not harvested." The historian Appian said that there was also famine around the time of the Battle of Philippi, in October 42 BCE, as "Thessaly was no longer able to furnish enough supplies" (*Bellum Civile* 4.122), and later he said that Rome was "devastated by famine" (*Bellum Civile* 5.25) (3). While such hardships probably spring in part from conflict and political turmoil, our evidence now suggests an additional strong environmental context.

The CESM simulations suggest that the Okmok II eruption in early 43 BCE resulted in 0.7 to 7.4^{o}C seasonal cooling in specific regions of southern Europe and northern Africa, with cooling especially pronounced during summer and autumn (SI Appendix, Figs. S8, S9). Although precipitation is often difficult to simulate accurately, model results also suggest that summer precipitation was 50 to 120% above normal throughout southern Europe, and autumn precipitation up to 400% percent of normal for specific regions, where normal is the average precipitation during the 60 to 46 BCE period with no volcanic forcing.

Other evidence for famine during this period comes from Egypt (3). Linkages between the agriculturally critical annual Nile River floods and political instability are well established (25-27), and particularly severe shocks to the Nile flood in the late 40s BCE are documented. The Okmok II eruption probably compounded the natural inter-annual variability of the Nile flood. Concomitant food shocks and the outbreak of disease are suggested in historical sources for the same years. Modern authorities agree that there were two famines in Egypt during the reign of Cleopatra, one of them occurring ca. 43-42 BCE. Seneca (*NQ* 4A.2.16) wrote that for two successive years, the tenth and eleventh of Cleopatra's reign (43 and 42 BCE), the Nile did not flood. Appian seemed to confirm this saying that in 43 BCE, Cleopatra declined to provide aid to Cassius on the grounds that Egypt was wracked by famine and pestilence (*Bellum Civile* 4.61); again (4.63) that Egypt was devastated by famine; and that around the time of the Battle of Philippi in October 42 BCE, Octavian and Antony could not obtain grain supplies from Egypt

because “the country was exhausted by famine” (4.108). Although Seneca and Appian were writing one and two centuries after the events, respectively, their testimony is corroborated by a contemporary inscription from Thebes in southern Egypt (*OGIS* 194; TM 6325). This honors the local governor Kallimachos for his assistance in a time of dearth that clearly lasted more than a year. The text probably dates to 39 BCE (Year 13 of Cleopatra’s reign), but referred to the continuing famine and social distress of the late 40s BCE.

The CESM simulations suggest sharp cooling from the Okmok II eruption in the lower reaches of the Nile River basin in spring, summer, and autumn, with little or no temperature change in the upper reaches (SI Appendix, Figs. S8, S9). The headwaters of the Blue Nile (and Atbara River) in the Ethiopian Highlands are the source of over 85% (28) of the annual Nile River floodwater, and connections are well described between explosive volcanism and the East African Monsoon (25, 29) that is responsible for much of the summer precipitation in the Highlands. The CESM simulations presented here suggest generally wetter winter conditions in the lower reaches of the Nile and substantially drier winter, spring, and especially autumn conditions in the upper reaches including the Blue Nile headwaters. Simulated summer precipitation in the Blue Nile headwaters, however, is unchanged or slightly higher as a result of the eruption.

The unusual atmospheric phenomena reported in Roman historical accounts in 44 BCE provide reasonable evidence for the presence of an aerosol veil in that year. We suggest that this probably was the result of the comparatively minor but local Mediterranean VEI 3 eruption of Mount Etna that year (2). Well-dated Arctic ice-core records of volcanic fallout provide clear evidence suggesting a massive eruption of Alaska’s Okmok volcano in early 43 BCE, thereby disassociating this eruption with the preceding aerosol veil, based upon the best available documentary and ice-core chronologies. This fallout coincided with a pronounced, two-year or longer period of much colder NH temperatures documented by climate proxy records and supported by Earth system climate modeling, with simulations also suggesting substantial changes in precipitation. In the Mediterranean region, these wet and extremely cold conditions during the agriculturally important spring through autumn seasons probably reduced crop yields starting in early 43 BCE and extending at least to early 41 BCE, compounding supply

problems wrought by the ongoing political upheavals of the period. That this indeed occurred is known from reporting of widespread food shortages and famine in the Roman provinces and Ptolemaic Kingdom.

Natural disasters are known historically to create a "state of exception" in which business as usual becomes unfeasible and political and cultural norms are suspended, thereby providing room for rapid social and political change (30). While it is difficult to establish direct causal linkages, we thus postulate that this extreme climate shock — among the most severe of the past 2,500 years — contributed to reported social unrest and facilitated political change at this important juncture of Western civilization. For example, Sextus Pompeius' naval blockade of Italy from late 43 to 36 BCE cutting off grain supplies from important grain-growing regions in Sicily, Africa, and elsewhere (Appian, *Bellum Civile* 5.15, 18; Dio Cassius 48.7.4) undoubtedly contributed to reported food shortages in Rome and throughout Roman Italy. Critical local food supplies (31), however, probably were already severely restricted by the extreme weather, and Sextus Pompeius can be seen as opportunistically using these circumstances to enhance political leverage arising from his blockade with constriction of much needed relief supplies. It is similarly challenging to establish direct links between Okmok II and the demise of the long-lasting Ptolemaic dynasty in Egypt, nominally accredited to the death of Cleopatra in 30 BC, following her naval defeat to Rome at the Battle of Actium in 31 BC. There can be little doubt, however, that Rome's interest in Egypt as its famed "breadbasket" was further magnified by the trials of the 40s BCE, and that Egypt's own capacity to defend against Rome was diminished by the famine, disease, land abandonment, and reduced state income that followed the Okmok II eruption.

Materials and Methods

Measurements of volcanic fallout in Arctic ice cores. Detailed elemental, chemical, and other (e.g., dielectric profiling [DEP] and electrical conductivity [ECM] reflecting acidity, laser light scattering [LLS] reflecting volcanic tephra) ice-core records reflecting volcanic fallout were evaluated for this study, with particular focus on the period from 50 to 30 BCE. Included were five Greenland ice cores (North Greenland Ice Core Project Two—NGRIP2 (7): 75.1°N, 42.3°W; North Greenland Eemian Ice Drilling (32) – NEEM: 77.5°N, 51.1°W; Greenland Ice Sheet Project

Two (9) – GISP2: 72.6°N, 38.5°W; Greenland Ice Core Project (33) – GRIP: 72.6°N, 37.6°W; DYE 3 (13): 65.18°N, 43.49°W), and one Russian Arctic (Akademii Nauk – AN (34): 80.5°N, 94.8°E) core. Note that because of uncertainties in ice-core chronologies between polar regions, a ~47(±5) BCE volcanic fallout (nssS) event in Antarctica (5) cannot be attributed conclusively to Okmok II.

Ice-core records of volcanic fallout included high-depth-resolution measurements of nssS and liquid conductivity in NGRIP2 (this study), NEEM (5, 32), and AN (this study), as well as size-resolved insoluble particle counts in NGRIP2 (this study) (SI Appendix, Fig. S1). Measurements were made with the unique continuous ice-core analytical system at DRI using methods described elsewhere (17, 35). Additional ice-core records included previously published, high-depth-resolution measurements of (1) DEP in NGRIP2 (36), NEEM (36), and GRIP (33), (2) ECM in GISP2 (37) and DYE3 (13), and (3) LLS in GISP2 (15). Note that the independently measured DEP records in NGRIP2 and NEEM were consistent with the continuous nssS and liquid conductivity measurements at DRI (SI Appendix, Fig. S1). We also evaluated discrete, two-year sulfate concentration measurements in GISP2 (9). Measurement techniques used to develop these previously published records were described elsewhere (13, 15, 33, 36, 37).

DRI_NGRIP2 ice-core chronology. To enable comparisons between ice-core volcanic fallout records, climate proxy information, and historical events, we used the precise DRI_NGRIP2 ice-core chronology and synchronized all the ice-core records to that chronology. Development of the NGRIP2 chronology has been described previously (7). Briefly, we used high-depth-resolution DRI measurements on the NGRIP2 core for multi-parameter annual-layer counting (SI Appendix, Fig. S2). Because the continuous DRI measurements began at 159.56 m corresponding to ~1270 CE, annual-layer counting started at unambiguous nssS fallout from the eruption of Samalas in 1257 CE (7). Evaluation of this independent chronology against well-established tree-ring-based chronologies using multi-annual (38) variations in cosmogenic nuclides (^{10}Be in ice, ^{14}C in wood) suggested uncertainty of less than ±2 years during antiquity. In addition, pronounced, short-lived cosmogenic nuclide increases in 994 CE and 775 CE

recorded in both tree and ice-core records (5) showed no offsets, indicating exact synchronization with the tree-based climate proxies at these specific dates (7). Moreover, recent evaluation of the DRI_NGRIP2 chronology using a newly discovered, short-lived cosmogenic nuclide event in the 1st millennium BCE (39) also showed no offset at 661 BCE (2610 ybp). Comparisons to the published NS1-2011 chronology (5) based largely on similar continuous DRI measurements in the 411 m NEEM-2011-S1 intermediate core and 390.5 to 573.65 m in the NEEM bedrock core, showed only minor differences (typically ±2 years), well within the uncertainties of the published NS1-2011 chronology. For example, fallout from the massive 43 BCE eruption using the DRI_NGRIP2 chronology occurred one year earlier in 44 BCE using the NS1-2011 chronology.

Fallout measurements in all six Arctic ice cores (Fig. 1; SI Appendix, Fig. S1) were synchronized at 43 BCE to allow comparisons. For NEEM, measurements on the NS1-2011 chronology were shifted by one year to align the 43 BCE event and an annual layer between 44 and 46 BCE on the original NS1-2011 deleted to align the 45 BCE event. Note that because of missing measurements, this annual layer was interpolated during development of the NS1-2011 chronology. For AN, pervasive surface melting and high marine biogenic inputs from the surrounding ocean made identification of volcanic sulfur spikes difficult. Acidity and nssS measurements were mapped to an existing chronology based primarily on tie points between heavy-metal concentrations in AN and the well-dated NGRIP2 record as previously described (8), and then shifted by ~2 years in this study to align the records at the start of the 43 BCE volcanic event. For GISP2, GRIP, and DYE3, measurements were mapped to the GICC05 timescale (40) and then compared to the NGRIP2 fallout record. Consistent with previous studies (5, 38), records on the GICC05 time scale (40) required a shift of ~10 years to align with the DRI_NGRIP2 chronology at the start of the 43 BCE event.

The speleothem-based summer temperature reconstruction from Shihua Cave (22), China was shifted by 2.5 years to synchronize at 43 BCE to be consistent with NH tree-ring-based climate proxies and the ice-core fallout records on the DRI_NGRIP2 chronology (Fig. 2). This shift was well within the five-year maximum counting error for the original speleothem chronology (22).

Tephra analyses. To determine the provenance of the fallout, we obtained a sample of archived GISP2 ice (481.06 to 481.16 m) from the National Science Foundation-Ice Core Facility (NSF-ICF) corresponding to the LLS spike at the start of the 43 BCE event (Fig. 2; SI Appendix, Fig. S3). The sample (QUB-1991) was melted and analyzed for tephra at Queen's University Belfast. The sample was centrifuged to concentrate particulates, decanted, and the residue transferred using plastic pipettes to a pre-ground, labeled glass slide on a hotplate within a laminar flow bench and when dry, covered in Buehler EpoxiCure 2 resin. The sample was scanned on a polarizing light microscope, and tephra shards counted and recorded. A total of 35 shards were identified (SI Appendix, Fig. S4), consisting of small (long axes mean 23 μm [ranging from 12 to 46 μm]), pale brown to brown, angular to sub-rounded glass (Fig. 3; SI Appendix, Fig. S5), with variable microlite content. The slide was then ground and polished to expose the surfaces of the tephra shards for geochemical analyses. Major element geochemistry was determined using combined electron and wavelength-dispersive spectrometry on a JEOL FEGSEM 6500F, with secondary glass standards analysed in the same sessions to ensure acceptable operating conditions. Eleven major and minor elements were analysed, following parameters previously outlined (41). Geochemical similarity to glass from the Okmok II caldera-forming eruption prompted analysis of reference glass from this event (SI Appendix, Fig. S5). Samples of lapilli (16JFLOK001F) and scoria (16JFLOK006A) from the eastern flank of Okmok corresponding to the second and third phases of the Okmok II event were ground, sieved, and prepared as thin sections on a glass slide for geochemical analysis on the JEOL FEGSEM 6500F under the same conditions as QUB-1991. All measurements were normalised to 100% to allow for water content.

Sulfur isotope analyses. GISP2 meltwater samples from 481.0 to 481.24 m were dried down and the sulfate isolated by column chemistry following established procedures (11). Sample sizes were small, with total sulfate ranging from 5 to 20 nmol. After purification, triple sulfur isotope (^{32}S, ^{33}S, ^{34}S) measurements were made by multi-collector Inductively Coupled Plasma Mass Spectrometry at the STAiG laboratory at the University of St. Andrews (11). $\Delta^{33}S$ values were calculated relative to the standard Vienna-Canyon Diablo Troilite (V-CDT)) as $\Delta^{33}S = \delta^{33}S + 1 - (\delta^{34}S + 1)^{0.515}$, where $\delta^{x}S = ({}^{x}S/{}^{32}S)_{sample}/({}^{x}S/{}^{32}S)_{VCDT} - 1$, with x either 33 or 34. Because of the

small samples sizes, 1σ uncertainties on $\Delta^{33}S$ ranged from 0.06 to 0.15‰ (SI Appendix, Fig. S3), slightly larger than previously reported uncertainties of 0.05‰ (11).

Earth System Model (ESM) simulations. We used the Community Earth System Model (CESM, version 1.2.2) (20) to evaluate the impact of the volcanic eruptions on NH climate. The model consists of coupled components for the atmosphere, ocean, land, and sea ice and is run in 2°×2° horizontal resolution in the atmosphere/land and 1°×1° in the ocean/sea ice. The vertical resolution of the atmosphere and ocean are 31 and 61 levels, respectively. A transient simulation started in year 1501 BCE was driven by orbital, solar (42), and greenhouse gas (43) forcing, as well as volcanic forcing. In 60 BCE, the transient simulation was branched to perform an ensemble of 10 CESM1.2.2 simulations. Small disturbances were introduced in the atmosphere at the first time step and run until 30 BCE with the prescribed volcanic forcing that included three NH eruptions in 45 BCE, 43 BCE (Okmok II), and 34 BCE.

Stratospheric volcanic sulfur injection estimates for the three eruptions between 60 and 30 BCE were taken from the eVolv2k database (44) which is based on quantification of Antarctic and Greenland sulfate depositional fluxes using bipolar ice-core arrays. The eruption years were shifted by one year to align with the DRI_NGRIP2 chronology and the default source locations from the eVolv2k database were adjusted to 64°N (i.e., Iceland) for the 45 BCE eruption and to 54.4°N for the Okmok eruption in 43 BCE. We also used an eruption date of January 1 based on a short time lag between the Okmok eruption and initial volcanic fallout in Greenland that started early 43 BCE. Using the Easy Volcanic Aerosol (EVA) forcing generator (45) and volcanic sulfur injection from eVolv2k, we generated global aerosol distributions and the evolution of extra-tropical stratospheric aerosol optical depth at 550nm. The space-time distribution of sulfate generated by EVA was converted to volcanic aerosol mass to be readable by CESM. Modifications to the prescribed aerosol distribution included (1) shifting peak sulfate injection in the stratosphere following (45) so that the atmospheric sulfate burden increased linearly until the fourth month after the eruption and then decreased exponentially according to the EVA model, and (2) increasing the volcanic aerosol mass by 45% to reconcile CESM and EVA optical depths following (46) but using the 1991 Pinatubo eruption as reference.

The model output consisted of monthly means that were combined to form a 10-ensemble average for evaluation of the volcanic climate effects. We calculated annual and seasonal (December to February [DJF], March to May [MAM], June to August [JJA], and September to November [SON]) anomalies from the monthly ensemble means after removing the seasonal variability, with the anomalies relative to the 60 through 46 BCE background period with no volcanic forcing. We used a student t-test (5% significance level or 2σ) to determine the significance of the anomalies relative to background variability during the reference period.

Data availability. All new high-resolution ice-core measurements presented in this study are provided in SI Dataset S01. Tephra geochemistry measurements are provided in SI Dataset S02.

Acknowledgements: National Science Foundation grants 1925417, 1023672, and 0909541 to J.R.M., and 1824770 to J.G.M. and F.M.L. funded this research, as well as support to A.I.W. and J.R.M. from the John Fell Oxford University Press (OUP) Research Fund and All Souls College, Oxford. Clare Hall, Cambridge provided additional support to J.R.M. through the Sir Nicholas Shackleton fellowship. F.M.L. also acknowledges support from an Irish Research Council Laureate Award (CLICAB project, IRCLA/2017/303). Swiss National Science Foundation grant 18001 funded C.C.R. and W.M.K. European Research Council grant 820047 under the European Union's Horizon 2020 research and innovation programme supported M.S. A.B. was supported by Marie Curie Career Integration Grant CIG14-631752. This work also benefitted from participation by some authors in the Past Global Changes (PAGES) Volcanic Impacts on Climate and Society (VICS) working group. We thank the NGRIP and NEEM communities, M. Twickler and the NSF-ICF for providing access to GISP2 samples, as well as students and staff in the DRI ice-core group for assistance in the laboratory. R. Kreidberg provided editorial advice.

Additional Information

Supporting information is available in the online version of the paper.

Competing financial interests

The authors declare no conflicts of interest.

Figure Legends

Figure 1. Location map. Shown are drilling sites for the six Arctic ice-core records evaluated in this study (+ symbols), the Okmok and Mt. Etna volcanoes, tree (6, 19) and Shihua Cave (22) speleothem-based climate proxy records, and the extent of the Roman provinces and Ptolemaic Kingdom in 44 BCE.

Figure 2. Ice-core, tree-ring, and speleothem evidence for the 45 and 43 BCE eruptions and climate effects. A) Selected historical and other events (see text). B) Model-simulated (gray) and observed (black) summer temperature anomalies from European tree-ring records with original 2σ uncertainties (6). C) Model-simulated (gray) and observed (black) summer temperature anomalies from the Chinese Shihua Cave speleothem record with original maximum temperature uncertainties (22). Shading in B) and C) shows annual CESM-ensemble standard errors. D) Continuous NGRIP2 and discrete (two-year) GISP2 nssS concentrations. E) NGRIP2 mass-equivalent insoluble particle concentrations for medium (2.5 to 5 µm) and large (5 to 10 µm) particles. F) GISP2 LLS measurements (15). G) Simulated 43 and 42 BCE average air-temperature anomalies (hashing shows anomalies that are not significant [2σ]). Annual and seasonal simulations for each year are shown in SI Appendix, Figs. S6, S7. All records were aligned at the start of the 43 BCE volcanic event to be consistent with the DRI_NGRIP2 chronology. Vertical shaded bar shows the extent of the insoluble particle (i.e., tephra) spike at the start of volcanic fallout in the NGRIP2 record.

Figure 3. Total alkali ($Na_2O + K_2O$) and silica compositions of tephra from GISP2 ice during the 43 BCE event compared with tephra from Okmok II and other potential source volcanoes. Filled circles show measurements (this study) of GISP2 and Okmok reference tephra. Shaded regions show tephra measurements from other potential first century BCE source volcanoes: Etna, Italy (47, 48); Chiltepe from Apoyeque, Nicaragua (49, 50); Masaya Triple Tuff (MTL), Nicaragua (49); A-2000, Askja, Iceland (51); White River Ash northern lobe (WRAn), Churchill, Canada (52); Furnas, Azores (53). Inset shows a tephra shard from the GISP2 sample. See SI Appendix, Fig. S5 for additional comparisons and analytical precision.

Figure 4. Volcanically forced temperature and precipitation anomalies in the Mediterranean region from 60 to 30 BCE. A) CESM-simulated average annual temperature and B) precipitation anomalies for 43 and 42 BCE, with outlines of Roman provinces north (red) and south (orange) of the Mediterranean. Dots show areas where annual anomalies are not significant (2σ) relative to the 60 to 46 BCE background variability with no volcanic forcing. Also shown are time series of simulated annual and seasonal temperature and precipitation anomalies for northern and southern Roman provinces. Years with symbols are significant (2σ) relative to the background variability. Gray bars show dates of ice-core-based volcanic sulfur injections (44) in the simulations, including the early 43 BCE Okmok II eruption.

References

1. J. Ramsey, A. Licht, *The Comet of 44 B.C. and Caesar's Funeral Games*. D. Blank, Ed., The American Philological Association (Scholars Press, Atlanta, Georgia, 1997).
2. R. Stothers, M. Rampino, Volcanic eruptions in the Mediterranean before A.D. 630 from written and archaeological sources. *Journal of Geophysical Research* **88**, 6357-6371 (1983).
3. P. Forsyth, In the wake of Etna, 44 B.C. *Classical Antiquity* **7**, 49-57 (1988).
4. D. Thompson, Cleopatra Queen of Egypt. *Ancient History* **17**, 11-15 (2018).
5. M. Sigl *et al.*, Timing and climate forcing of volcanic eruptions for the past 2,500 years. *Nature* **523**, 543–549 (2015).
6. J. Luterbacher *et al.*, European summer temperatures since Roman times. *Environmental Research Letters* **11** (2016).
7. J. McConnell *et al.*, Lead pollution recorded in Greenland ice indicates European emissions tracked plagues, wars, and imperial expansion during antiquity. *Proceedings of the National Academy of Sciences of the United States of America* **115**, 5726-5731 (2018).
8. J. McConnell *et al.*, Pervasive Arctic lead pollution suggests substantial growth in medieval silver production modulated by plague, climate, and conflict. *Proceedings of the National Academy of Sciences of the United States of America* **116**, 14910-14915 (2019).
9. G. Zielinski *et al.*, Record of volcanism since 7000 B.C. from the GISP2 Greenland ice core and implications for the volcano-climate system. *Science* **264**, 948-952 (1994).
10. K. Harper, In the shadow of Caesar. *Lapham's Quarterly* (2019).
11. A. Burke *et al.*, Stratospheric eruptions from tropical and extra-tropical volcanoes constrained using high-resolution sulfur isotopes in ice cores. *Earth and Planetary Science Letters* **521**, 113-119 (2019).
12. G. Zielinski, G. Mershon, Paleoenvironmental implications of the insoluble microparticle record in the GISP2 (Greenland) ice core during the rapidly changing climate of the Pleistocene-Holocene transition. *Geological Society of America Bulletin* **109**, 547-559 (1997).
13. H. Clausen *et al.*, A comparison of the volcanic records over the past 4000 years from the Greenland Ice Core Project and Dye 3 Greenland Ice Cores. *Journal of Geophysical Research-Oceans* **102**, 26707-26723 (1997).
14. C. Plummer *et al.*, An independently dated 2000-yr volcanic record from Law Dome, East Antarctica, including a new perspective on the dating of the 1450s CE eruption of Kuwae, Vanuatu. *Climate of the Past* **8**, 1929-1940 (2012).
15. M. Ram, G. Koenig, Continuous dust concentration profile of pre-Holocene ice from the Greenland Ice Sheet Project 2 ice core: Dust stadials, interstadials, and the Eemian. *Journal of Geophysical Research-Oceans* **102**, 26641-26648 (1997).
16. N. Dunbar *et al.*, New Zealand supereruption provides time marker for the Last Glacial Maximum in Antarctica. *Scientific Reports* **7** (2017).
17. J. McConnell *et al.*, Synchronous volcanic eruptions and abrupt climate change ~17.7 ka plausibly linked by stratospheric ozone depletion. *Proceedings of the National Academy of Sciences of the United States of America* **114**, 10035-10040 (2017).

18. J. Larsen, C. Neal, J. Schaefer, J. Biget, C. Nye, Late Pleistocene and Holocene caldera-forming eruptions of Okmok Caldera, Aleutian Islands, Alaska. *Geophysical Monograph Series* **172** (2007).
19. V. LaMarche, K. Hirschboeck, Frost rings in trees as records of major volcanic eruptions. *Nature* **307**, 121-126 (1984).
20. J. Hurrell *et al.*, The Community Earth System Model A Framework for Collaborative Research. *Bulletin of the American Meteorological Society* **94**, 1339-1360 (2013).
21. J. Esper, E. Duthorn, P. Krusic, M. Timonen, U. Buntgen, Northern European summer temperature variations over the Common Era from integrated tree-ring density records. *Journal of Quaternary Science* **29**, 487-494 (2014).
22. M. Tan *et al.*, Cyclic rapid warming on centennial-scale revealed by a 2650-year stalagmite record of warm season temperature. *Geophysical Research Letters* **30** (2003).
23. D. Zhang, *A compendium of Chinese meteorological records of the last 3,000 years* (Jiangsu Education Publishing House, Nanjing, 2004).
24. P. Garnsey, *Famine and food supply in the Graecco-Roman world: responses to risk and crisis* (Cambridge University Press, Cambridge, 1988), pp. 303.
25. L. Oman, A. Robock, G. Stenchikov, T. Thordarson, High-latitude eruptions cast shadow over the African monsoon and the flow of the Nile. *Geophysical Research Letters* **33** (2006).
26. J. Manning *et al.*, Volcanic suppression of Nile summer flooding triggers revolt and constrains interstate conflict in ancient Egypt. *Nature Communications* **8** (2017).
27. E. Chaney, Revolt on the Nile: Economic shocks, religion, and political power. *Econometrica* **81**, 2033-2053 (2013).
28. A. M. Melesse, S. Bekele, P. McCormick, "Introduction: Hydrology of the Niles in the Face of Climate and Land-Use Dynamics" in Nile River Basin: Hydrology, Climate and Water Use A. M. Melesse, Ed. (Springer, Berlin, 2011), pp. vii-xvii.
29. C. Colose, A. LeGrande, M. Vuille, Hemispherically asymmetric volcanic forcing of tropical hydroclimate during the last millennium. *Earth System Dynamics* **7**, 681-696 (2016).
30. M. R. Dove, *Anthropology of Climate Change: An Historical Reader* (Wiley & Sons, Chichester, 2014).
31. P. Erdkamp, *The Grain Market in the Roman Empire* (Cambridge University Press, Cambridge, 2005), pp. 364.
32. M. Sigl *et al.*, A new bipolar ice core record of volcanism from WAIS Divide and NEEM and implications for climate forcing of the last 2000 years. *Journal of Geophysical Research-Atmospheres* **118**, 1151-1169 (2013).
33. E. Wolff, J. Moore, H. Clausen, C. Hammer, Climatic implications of background acidity and other chemistry derived from electrical studies of the Greenland Ice Core Project ice core. *Journal of Geophysical Research-Oceans* **102**, 26325-26332 (1997).
34. T. Opel, D. Fritzsche, H. Meyer, Eurasian Arctic climate over the past millennium as recorded in the Akademii Nauk ice core (Severnaya Zemlya). *Climate of the Past* **9**, 2379-2389 (2013).
35. J. R. McConnell, Continuous ice-core chemical analyses using inductively Coupled Plasma Mass Spectrometry. *Environmental Science & Technolology* **36**, 7-11 (2002).
36. S. Mojtabavi *et al.*, A first chronology for the East GReenland Ice–core Project (EGRIP) over the Holocene and last glacial termination. *Climate of the Past Discussions* (2019).

37. K. Taylor, R. Alley, G. Lamorey, P. Mayewski, Electrical measurements on the Greenland Ice Sheet Project 2 core. *Journal of Geophysical Research-Oceans* **102**, 26511-26517 (1997).
38. F. Adolphi, R. Muscheler, Synchronizing the Greenland ice core and radiocarbon timescales over the Holocene – Bayesian wiggle-matching of cosmogenic radionuclide records. *Climate of the Past* **12**, 15-30 (2016).
39. P. O'Hare *et al.*, Multiradionuclide evidence for an extreme solar proton event around 2,610 BP (similar to 660 BC). *Proceedings of the National Academy of Sciences of the United States of America* **116**, 5961-5966 (2019).
40. I. Seierstad *et al.*, Consistently dated records from the Greenland GRIP, GISP2 and NGRIP ice cores for the past 104 ka reveal regional millennial-scale delta O-18 gradients with possible Heinrich event imprint. *Quaternary Science Reviews* **106**, 29-46 (2014).
41. S. Coulter *et al.*, Holocene tephras highlight complexity of volcanic signals in Greenland ice cores. *Journal of Geophysical Research-Atmospheres* **117** (2012).
42. G. Schmidt *et al.*, Climate forcing reconstructions for use in PMIP simulations of the Last Millennium (v1.1). *Geoscientific Model Development* **5**, 185-191 (2012).
43. F. Joos, R. Spahni, Rates of change in natural and anthropogenic radiative forcing over the past 20,000 years. *Proceedings of the National Academy of Sciences of the United States of America* **105**, 1425-1430 (2008).
44. M. Toohey, M. Sigl, Volcanic stratospheric sulfur injections and aerosol optical depth from 500 BCE to 1900 CE. *Earth System Science Data* **9**, 809-831 (2017).
45. C. Gao, A. Robock, C. Ammann, Volcanic forcing of climate over the past 1500 years: An improved ice core-based index for climate models. *Journal of Geophysical Research-Atmospheres* **113** (2008).
46. Y. Zhong, A. Jahn, G. Miller, A. Geirsdottir, Asymmetric Cooling of the Atlantic and Pacific Arctic During the Past Two Millennia: A Dual Observation-Modeling Study. *Geophysical Research Letters* **45**, 12497-12505 (2018).
47. L. Sadori, B. Narcisi, The Postglacial record of environmental history from Lago di Pergusa, Sicily. *Holocene* **11**, 655-671 (2001).
48. H. Vogel, G. Zanchetta, R. Sulpizio, B. Wagner, N. Nowaczyk, A tephrostratigraphic record for the last glacial-interglacial cycle from Lake Ohrid, Albania and Macedonia. *Journal of Quaternary Science* **25**, 320-338 (2010).
49. S. Kutterolf *et al.*, Pacific offshore record of plinian arc volcanism in Central America: 1. Along-arc correlations. *Geochemistry Geophysics Geosystems* **9** (2008).
50. S. Kutterolf, A. Freundt, C. Burkert, Eruptive history and magmatic evolution of the 1.9 kyr Plinian dacitic Chiltepe Tephra from Apoyeque volcano in west-central Nicaragua. *Bulletin of Volcanology* **73**, 811-831 (2011).
51. K. Barber, P. Langdon, A. Blundell, Dating the Glen Garry tephra: a widespread late-Holocene marker horizon in the peatlands of northern Britain. *Holocene* **18**, 31-43 (2008).
52. S. Preece *et al.*, Chemical complexity and source of the White River Ash, Alaska and Yukon. *Geosphere* **10**, 1020-1042 (2014).
53. S. Wastegård, H. Johansson, J. Pacheco, New major element analyses of proximal tephras from the Azores and suggested correlations with cryptotephras in northwest Europe. *Journal of Quaternary Science* **35**, 114-121 (2020).

Figure 1.

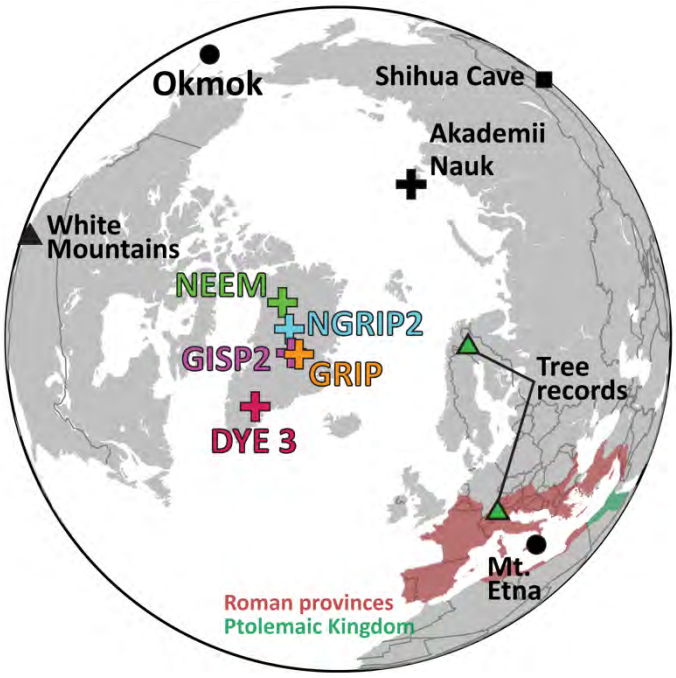
Okmok
Shihua Cave
Akademii
Nauk
White
Mountains
NEEM
NGRIP2
GISP2
GRIP
DYE 3
Tree
records
Mt.
Etna
Roman provinces
Ptolemaic Kingdom

Figure 2.

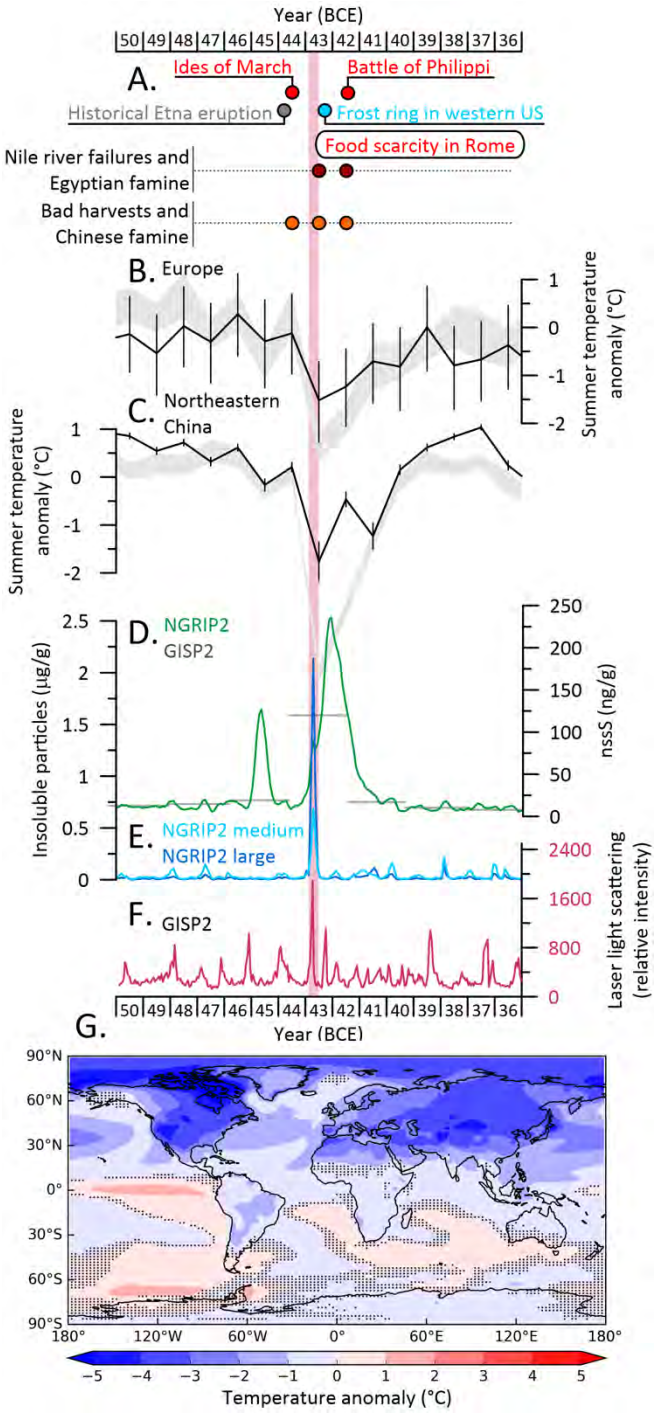

Figure 3.

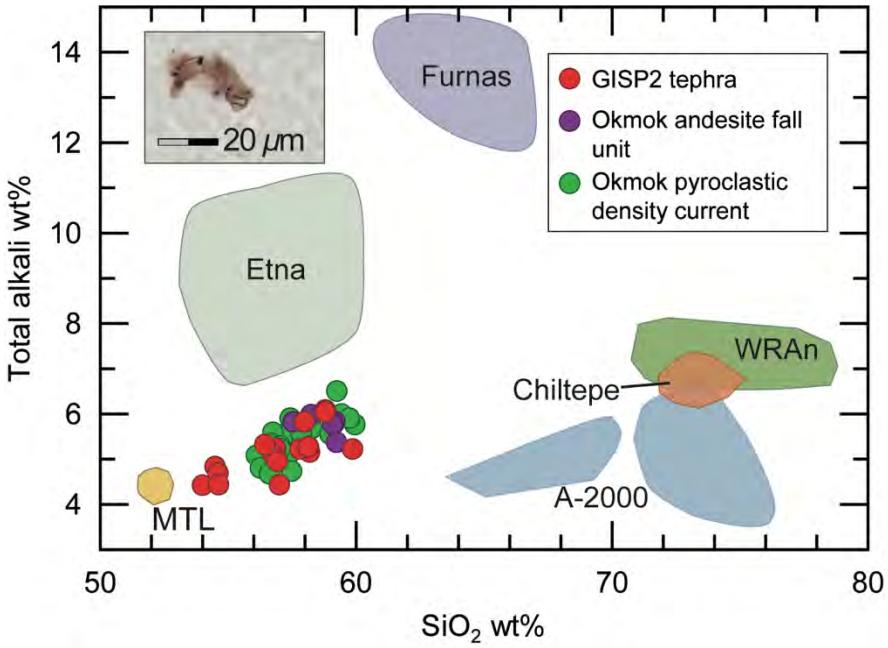

Figure 4.

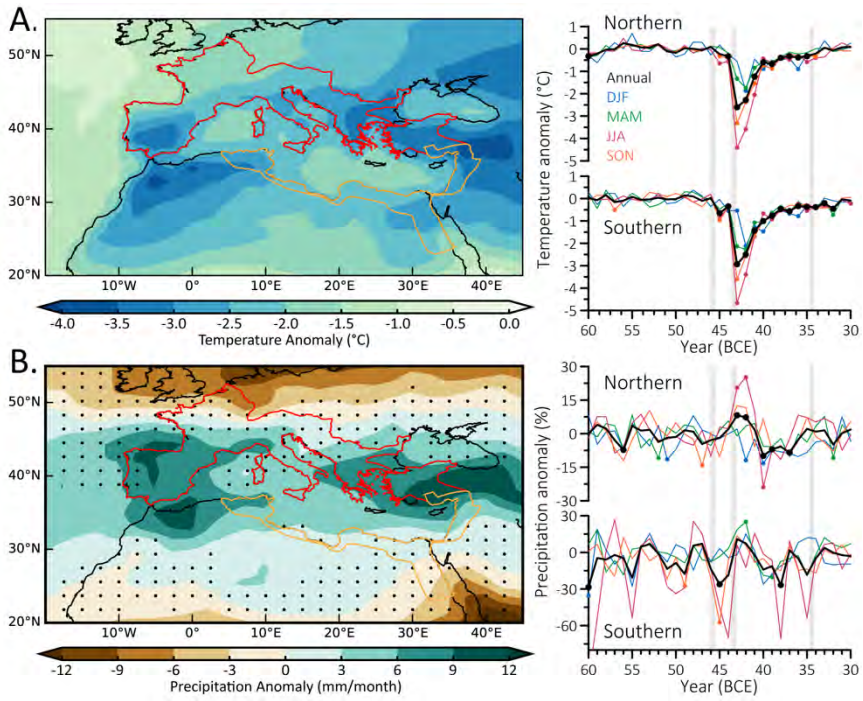

SI Appendix

Extreme climate after massive eruption of Alaska's Okmok volcano in 43 BCE and effects on the late Roman Republic and Ptolemaic Kingdom

Joseph R. McConnell, Michael Sigl, Gill Plunkett, Andrea Burke, Woon Mi Kim, Christoph C. Raible, Andrew I. Wilson, Joseph G. Manning, Francis M. Ludlow, Nathan J. Chellman, Helen M. Innes, Zhen Yang, Jessica F. Larsen, Janet R. Schaefer, Sepp Kipfstuhl, Seyedhamidreza Mojtabavi, Frank Wilhelms, Thomas Opel, Hanno Meyer, Jørgen Peder Steffensen

Corresponding author: Joseph R. McConnell, joe.mcconnell@dri.edu

Contents

Other supplementary materials

1. Dataset S01.xlsx contains ice-core data in Fig. 2 and SI Appendix, Figs. S1, S2, and S3.
2. Dataset S02.xlsx contains tephra data in Fig. 3 and SI Appendix, Fig. S5.

Table S1. DRI_NGRIP2 age scale in both year before 1950 (yb1950) and year (BCE/CE). Shading identifies approximate periods in the NGRIP2 and NEEM cores of high (>3 σ above background) non-sea-salt sulfur concentration indicating elevated volcanic fallout.

yb1950 (ybp)	BCE(-)/CE(+)	Approximate Date
1948	+2	Jan-01
1948.25	+1	Oct-01
1948.5	+1	Jul-01
1948.75	+1	Apr-01
1949	+1	Jan-01
1949.25	-1	Oct-01
1949.5	-1	Jul-01
1949.75	-1	Apr-01
1950	-1	Jan-01
1950.25	-2	Oct-01
1989	-40	Jan-01
1989.25	-41	Oct-01
1989.5	-41	Jul-01
1989.75	-41	Apr-01
1990	-41	Jan-01
1990.25	-42	Oct-01
1990.5	-42	Jul-01
1990.75	-42	Apr-01
1991	-42	Jan-01
1991.25	-43	Oct-01
1991.5	-43	Jul-01
1991.75	-43	Apr-01
1992	-43	Jan-01
1992.25	-44	Oct-01
1992.5	-44	Jul-01
1992.75	-44	Apr-01
1993	-44	Jan-01
1993.25	-45	Oct-01
1993.5	-45	Jul-01
1993.75	-45	Apr-01
1994	-45	Jan-01
1994.25	-46	Oct-01

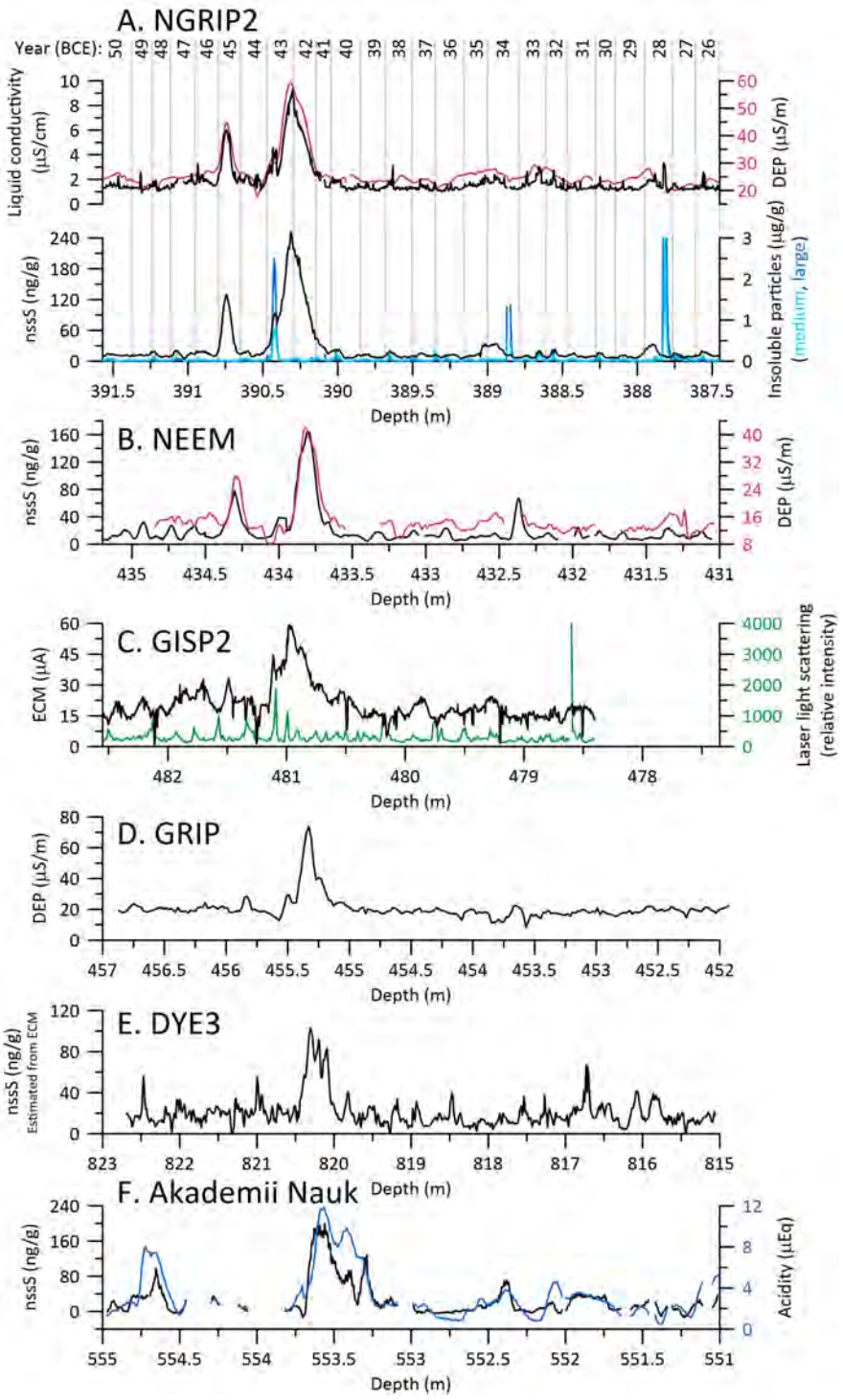

Figure S1. Selected new and previously published measurements of volcanic-fallout-related parameters in the six Arctic ice cores (Fig. 1) evaluated for this study: A. NGRIP2 (this study and (1)), B. NEEM ((1, 2), C. GISP2 (3-5), D. GRIP (6, 7), E. DYE3 (6), and F. Akademii Nauk (this study). Depth ranges correspond approximately to 25 to 50 BCE after synchronization at 43 BCE to the DRI-NGRIP2 age scale (8).

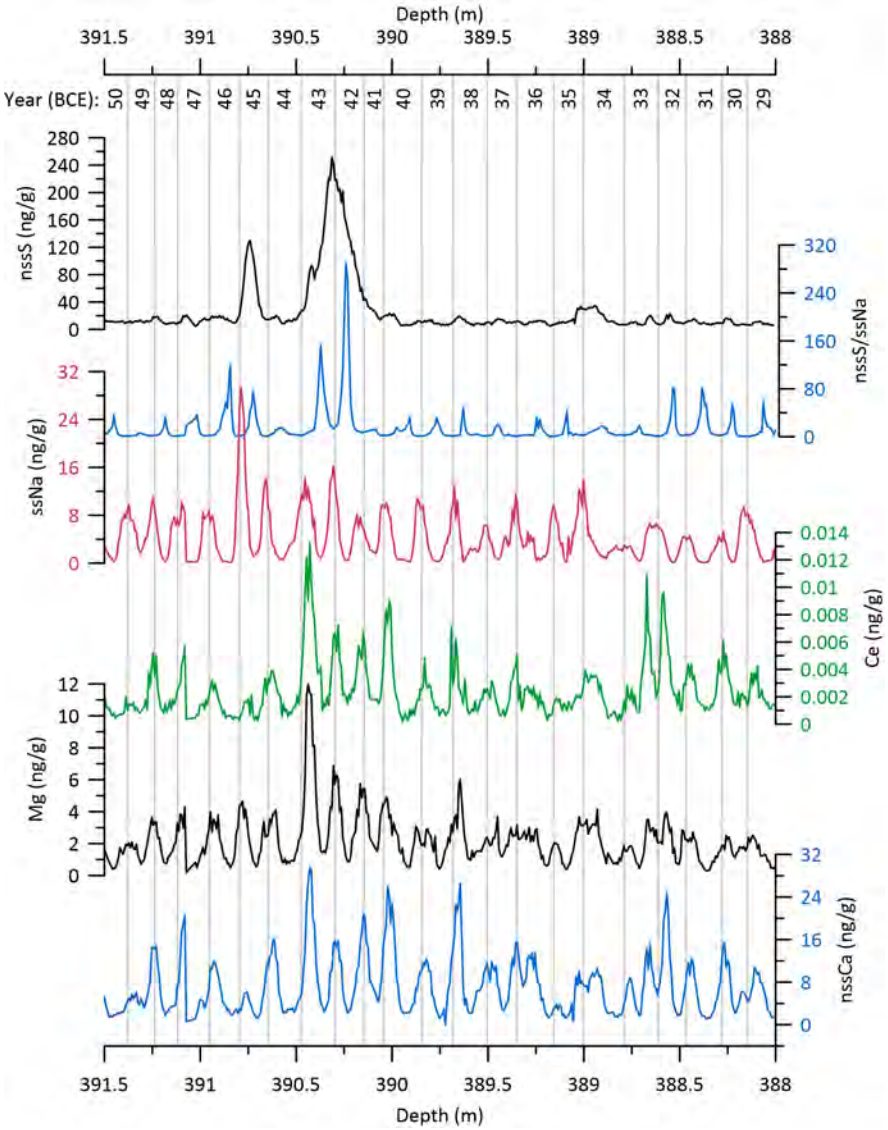

Figure S2. Selected continuous elemental measurements of NGRIP2 ice (388 to 391.5 m) used for annual layer counting. Shown are nssS, the ratio of nssS/ssNa, ssNa, cerium (Ce), magnesium (Mg), and nssCa, where nssS is non-sea-salt sulfur, ssNa is sea-salt sodium, and nssCa is non-sea-salt calcium. Also shown are mid-winter (ostensibly January 1) annual layer picks corresponding to 29 BC to 49 BCE on the DRI_NGRIP2 age scale (8). Ce and nssCa are primarily continental dust indicators while Mg includes both sea-salt and dust components. nssS reflects both volcanic fallout and background marine and terrestrial biogenic emissions.

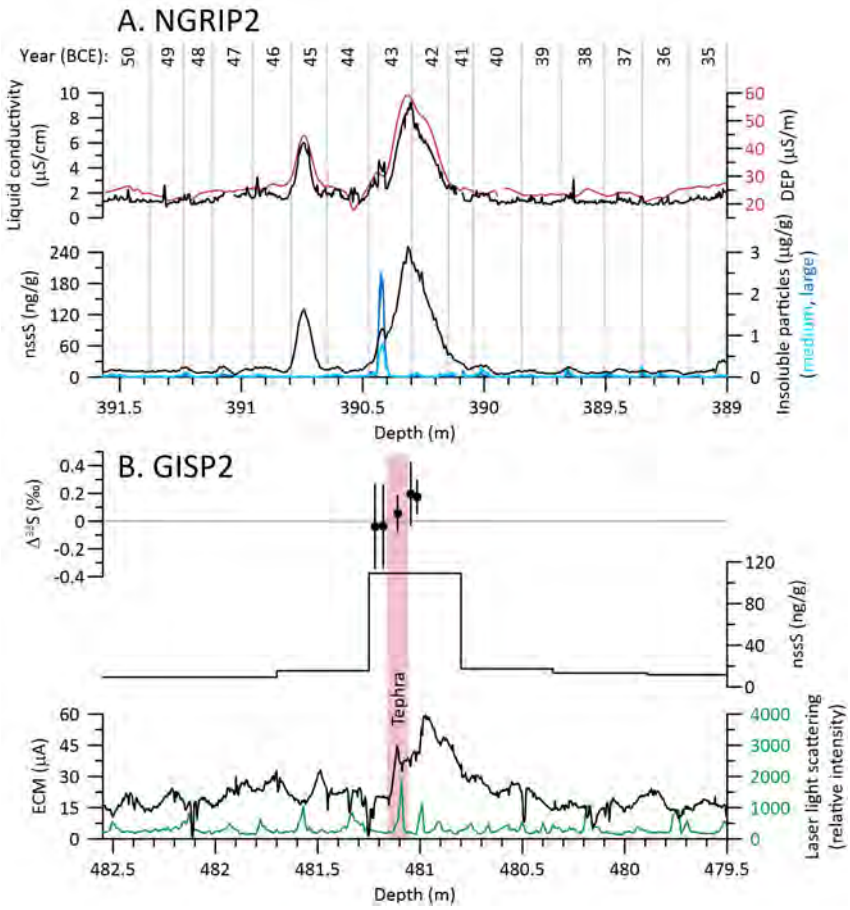

Figure S3. Volcanic fallout surrounding the 43 BCE Okmok II eruption in the A. NGRIP2 and B. GISP2 ice cores. Shown for NGRIP2 are continuous measurements of liquid conductivity (this study), field DEP (1), nssS (this study) and medium (2.5 to 5 µm) and large (5 to 10 µm) insoluble particle counts (this study). Shown for GISP2 are discrete measurements of $\Delta^{33}S$ (±2σ) (this study), discrete sulfate (4), ECM (3), and laser light scattering (9). Tephra used to identify Okmok II as the source eruption were filtered from an ice sample extending from 481.06 to 481.16 m depth (vertical shaded bar) from the GISP2 core.

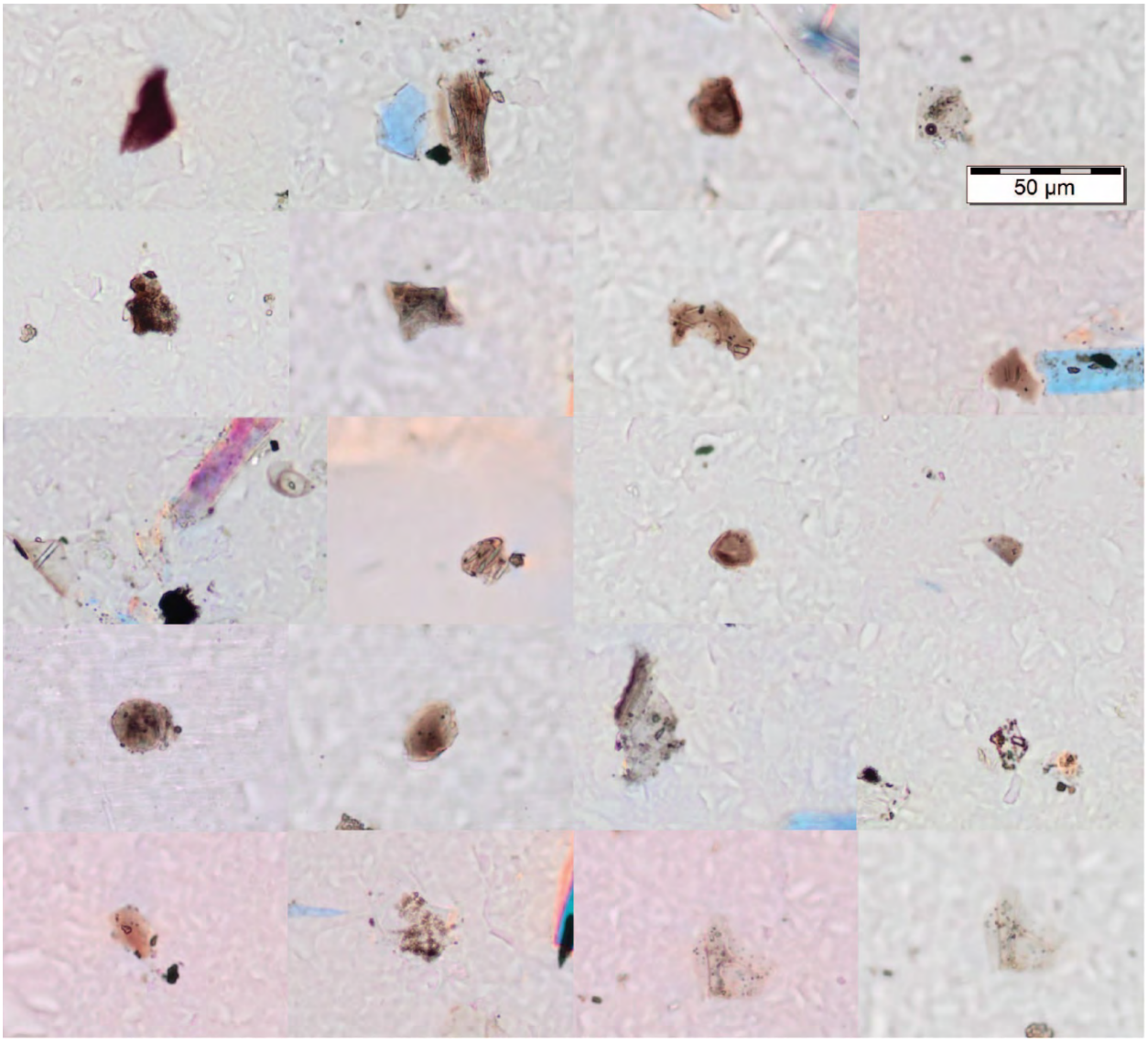

Figure S4. Images of selected tephra shards extracted from GISP2 ice (481.06 to 481.16 m) and geochemically tied to the Okmok II eruption that started in early 43 BCE.

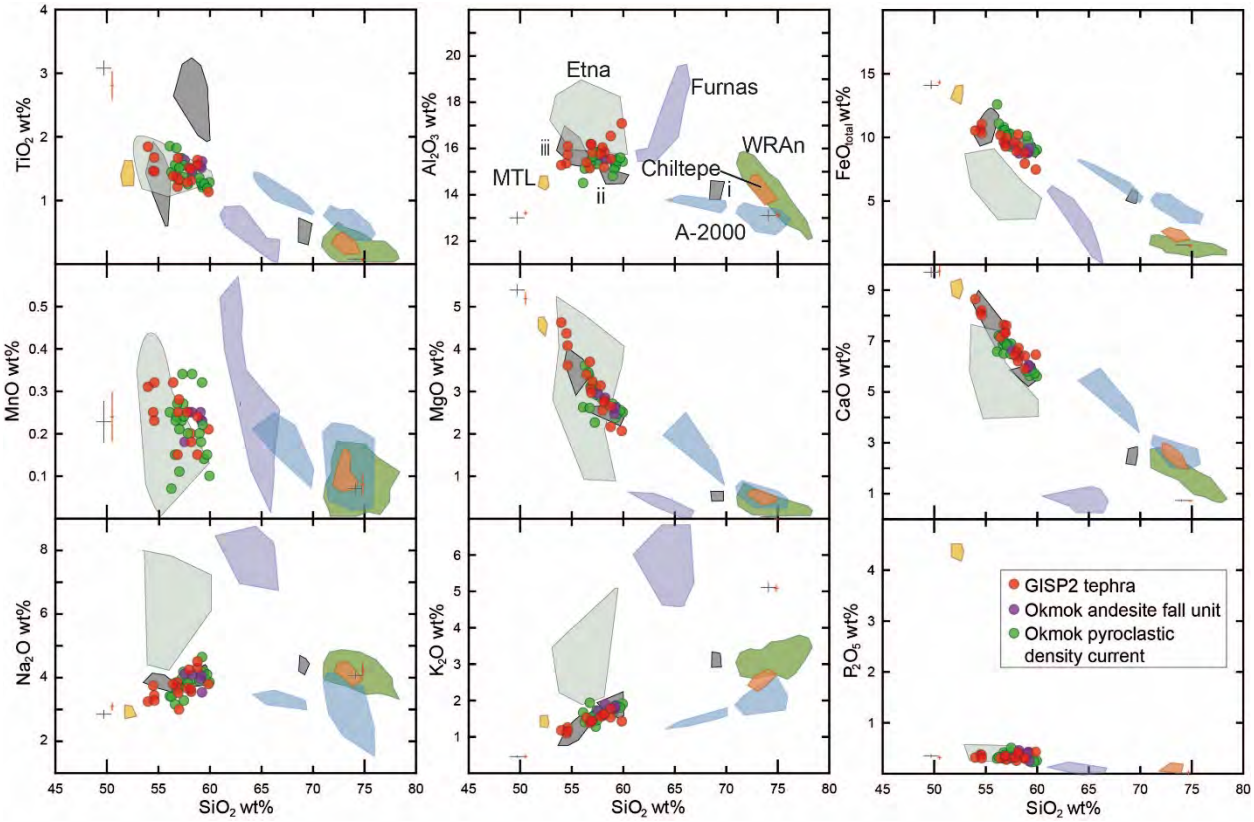

Figure S5. Tephra geochemistry comparisons between shards extracted from GISP2 ice (481.06 to 481.16 m) and potential NH source eruptions including Etna, as well as large eruptions thought within dating uncertainties to have occurred in the 1st century BCE. Filled circles show measurements (this study) of GISP2 and Okmok reference tephra (Materials and Methods; Dataset S02). Shaded regions show tephra reference measurements from other potential source volcanoes: Etna, Italy (10, 11); Chiltepe from Apoyeque, Nicaragua (12, 13); Masaya Triple Tuff (MTL), Nicaragua (12); A-2000, Askja, Iceland (14); White River Ash northern lobe (WRAn), Churchill, Canada (15); Furnas, Azores (16). Gray shading shows prior measurements of tephra samples from the first (i.), second (ii.) and third (iii.) eruption phases of Okmok II (17). Analytical precision for the GISP2/Okmok measurements is illustrated by the red crosses representing 2σ of repeated analyses of the secondary glass standards (high Si – Lipari, low Si - Laki); for comparison, accepted values for Lipari and Laki (2 σ) (18) are shown by the grey crosses.

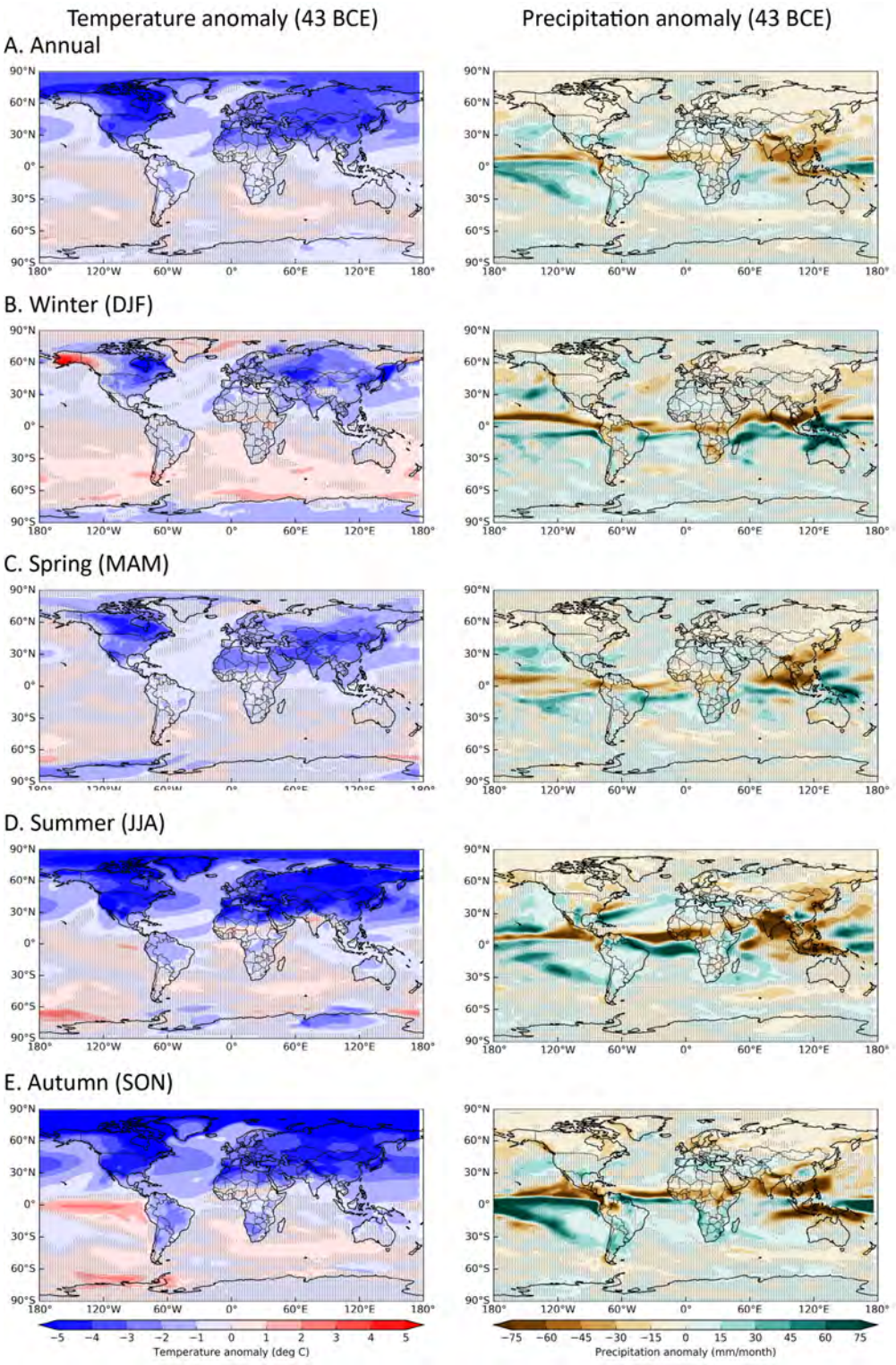

Figure S6. Annual and seasonal 43 BCE CESM-modeled (Materials and Methods) temperature and precipitation anomalies relative to the 60 to 46 BCE reference period with no volcanic forcing. Dots show areas where the anomalies are not significant (2σ) relative to the background variability.

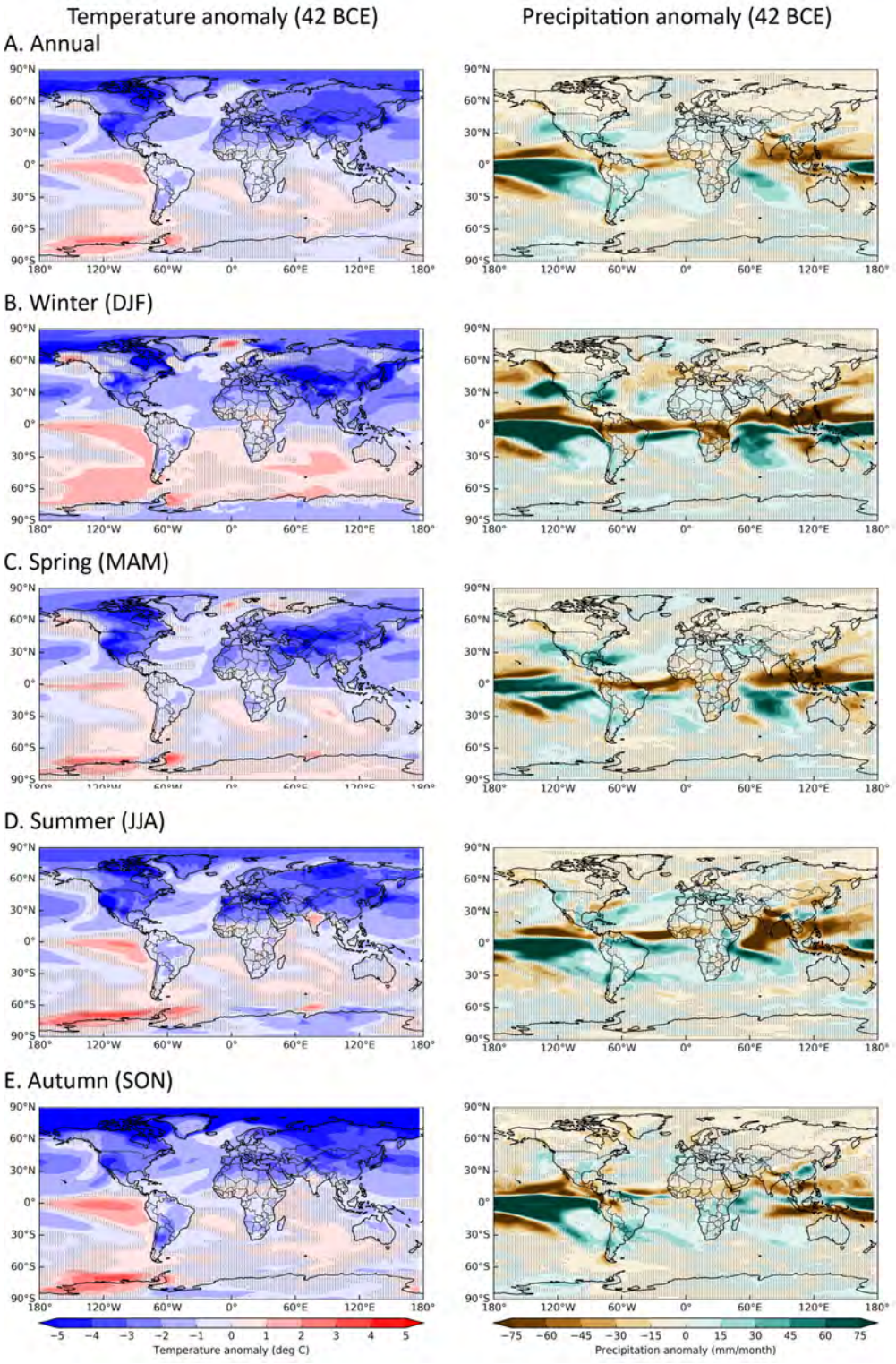

Figure S7. As in SI Appendix, Fig. S6 but for 42 BCE.

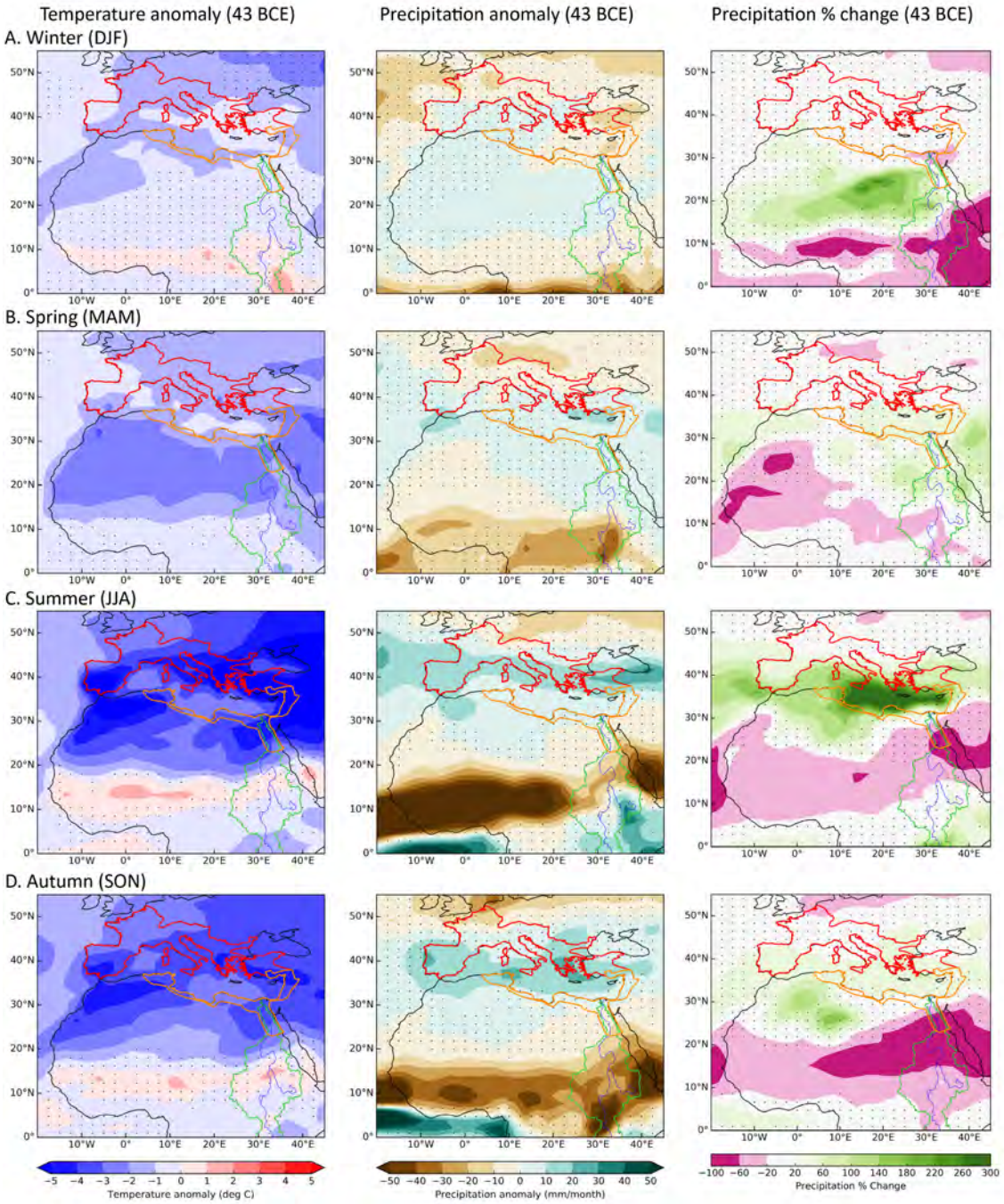

Figure S8. Seasonal 43 BCE CESM-modeled (Materials and Methods) temperature and precipitation anomalies in response to radiative forcing from the early 43 BCE Okmok II eruption. Outlines show (red) Roman provinces north of the Mediterranean, (orange) Ptolemaic Kingdom and Roman provinces south of the Mediterranean, and (green) the Nile River drainage. Anomalies and precipitation change are relative to the 60 to 46 BCE reference period with no volcanic forcing. Dots show areas where the anomalies are not significant (2σ) relative to the background variability.

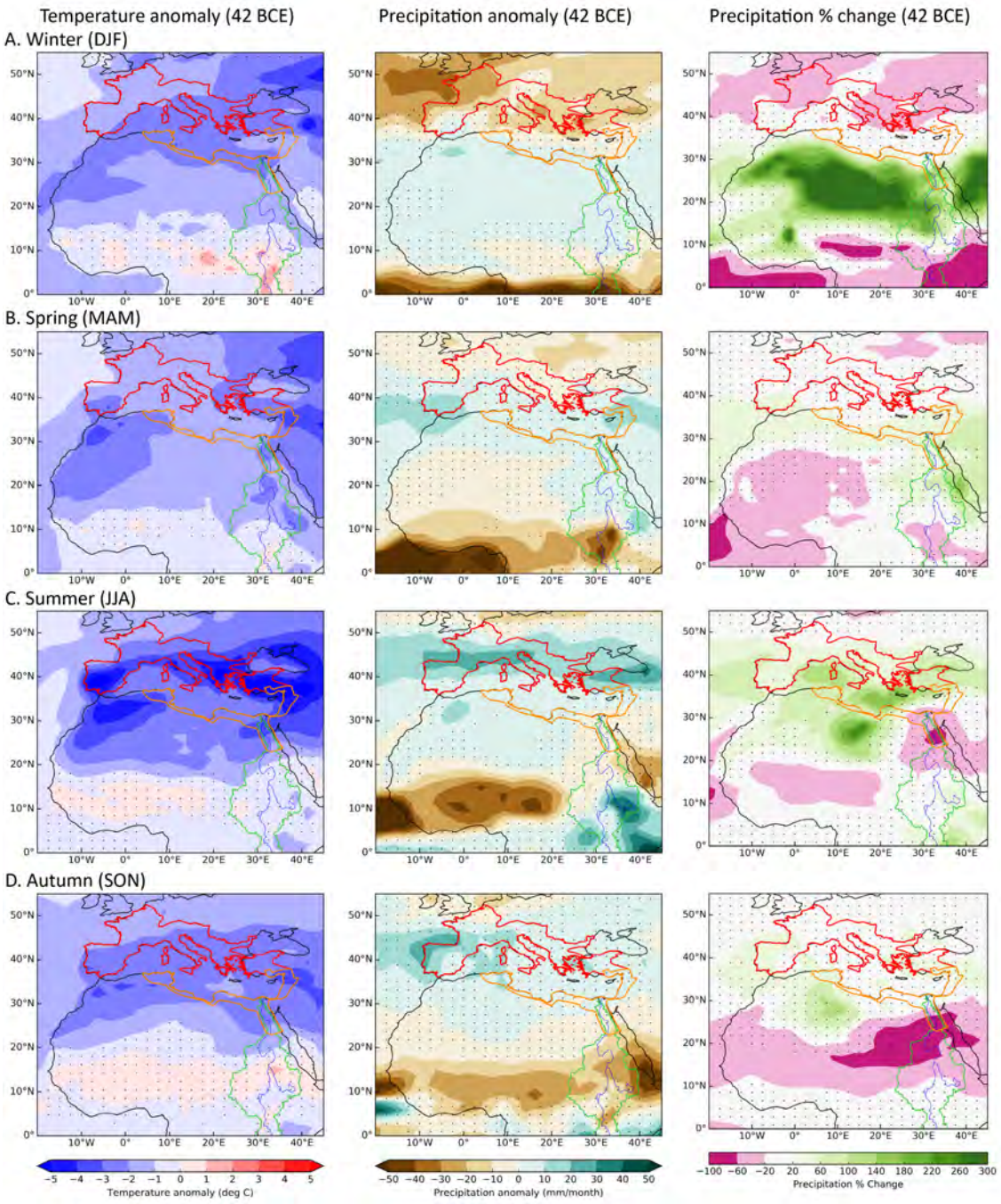

Figure S9. As in SI Appendix, Fig. S8 but for 42 BCE.

Supplemental Information References

1. S. Mojtabavi *et al.*, A first chronology for the East GReenland Ice–core Project (EGRIP) over the Holocene and last glacial termination. *Climate of the Past Discussions* (2019).
2. M. Sigl *et al.*, Timing and climate forcing of volcanic eruptions for the past 2,500 years. *Nature* **523**, 543–549 (2015).
3. K. Taylor, R. Alley, G. Lamorey, P. Mayewski, Electrical measurements on the Greenland Ice Sheet Project 2 core. *Journal of Geophysical Research-Oceans* **102**, 26511-26517 (1997).
4. G. Zielinski *et al.*, Record of volcanism since 7000 B.C. from the GISP2 Greenland ice core and implications for the volcano-climate system. *Science* **264**, 948-952 (1994).
5. G. Zielinski, G. Mershon, Paleoenvironmental implications of the insoluble microparticle record in the GISP2 (Greenland) ice core during the rapidly changing climate of the Pleistocene-Holocene transition. *Geological Society of America Bulletin* **109**, 547-559 (1997).
6. H. Clausen *et al.*, A comparison of the volcanic records over the past 4000 years from the Greenland Ice Core Project and Dye 3 Greenland Ice Cores. *Journal of Geophysical Research-Oceans* **102**, 26707-26723 (1997).
7. E. Wolff, J. Moore, H. Clausen, C. Hammer, Climatic implications of background acidity and other chemistry derived from electrical studies of the Greenland Ice Core Project ice core. *Journal of Geophysical Research-Oceans* **102**, 26325-26332 (1997).
8. J. McConnell *et al.*, Lead pollution recorded in Greenland ice indicates European emissions tracked plagues, wars, and imperial expansion during antiquity. *Proceedings of the National Academy of Sciences of the United States of America* **115**, 5726-5731 (2018).
9. M. Ram, G. Koenig, Continuous dust concentration profile of pre-Holocene ice from the Greenland Ice Sheet Project 2 ice core: Dust stadials, interstadials, and the Eemian. *Journal of Geophysical Research-Oceans* **102**, 26641-26648 (1997).
10. L. Sadori, B. Narcisi, The Postglacial record of environmental history from Lago di Pergusa, Sicily. *Holocene* **11**, 655-671 (2001).
11. H. Vogel, G. Zanchetta, R. Sulpizio, B. Wagner, N. Nowaczyk, A tephrostratigraphic record for the last glacial-interglacial cycle from Lake Ohrid, Albania and Macedonia. *Journal of Quaternary Science* **25**, 320-338 (2010).
12. S. Kutterolf *et al.*, Pacific offshore record of plinian arc volcanism in Central America: 1. Along-arc correlations. *Geochemistry Geophysics Geosystems* **9** (2008).
13. S. Kutterolf, A. Freundt, C. Burkert, Eruptive history and magmatic evolution of the 1.9 kyr Plinian dacitic Chiltepe Tephra from Apoyeque volcano in west-central Nicaragua. *Bulletin of Volcanology* **73**, 811-831 (2011).
14. K. Barber, P. Langdon, A. Blundell, Dating the Glen Garry tephra: a widespread late-Holocene marker horizon in the peatlands of northern Britain. *Holocene* **18**, 31-43 (2008).
15. S. Preece *et al.*, Chemical complexity and source of the White River Ash, Alaska and Yukon. *Geosphere* **10**, 1020-1042 (2014).

16. S. Wastegård, H. Johansson, J. Pacheco, New major element analyses of proximal tephras from the Azores and suggested correlations with cryptotephras in northwest Europe. *Journal of Quaternary Science* **35**, 114-121 (2020).
17. J. Larsen, C. Neal, J. Schaefer, J. Biget, C. Nye, Late Pleistocene and Holocene caldera-forming eruptions of Okmok Caldera, Aleutian Islands, Alaska. *Geophysical Monograph Series* **172** (2007).
18. S. Kuehn, D. Froese, P. Shane, I. INTAV Intercomparison Participants, The INTAV intercomparison of electron-beam microanalysis of glass by tephrochronology laboratories: Results and recommendations. *Quaternary International* **246**, 19-47 (2011).